Journal of Alloys and Compounds 563 (2013) 254–260

Contents lists available at SciVerse ScienceDirect

Journal of Alloys and Compounds

journal homepage: www.elsevier.com/locate/jalcom

Influence of the indium concentration on microstructural and electrical properties of proton conducting NiO–$BaCe_{0.9-x}In_xY_{0.1}O_{3-\delta}$ cermet anodes for IT-SOFC application

Milan Zunic [a,b,*], Goran Brankovic [b], Cesar Renato Foschini [a], Mario Cilense [a], Elson Longo [a], José Arana Varela [a]

[a] Instituto de Quimica, UNESP–LIEC, CMDMC, Rua Prof. Francisco Degni, 55, CEP 14800-900, Araraquara, SP, Brazil
[b] Institute for Multidisciplinary Research, University of Belgrade, Kneza Viseslava 1, 11000 Belgrade, Serbia

ARTICLE INFO

Article history:
Received 19 November 2012
Received in revised form 14 February 2013
Accepted 16 February 2013
Available online 1 March 2013

Keywords:
Fuel cells
Anode
Cermet
Protonic conductor

ABSTRACT

Optimization of the major properties of anodes based on proton conductors, such as microstructure, conductivity and chemical stability, is yet to be achieved. In this study we investigated the influence of indium on the chemical stability, microstructural and electrical characteristics of proton conducting NiO–$BaCe_{0.9-x}In_xY_{0.1}O_{3-\delta}$ (NiO–BCIYx) anodes. Four compositions of cermet anode substrates NiO–BCIYx were prepared using the method of evaporation and decomposition of solutions and suspensions (EDSS). Sintered anode substrates were reduced and their microstructural and electrical properties were examined before and after reduction as a function of the amount of indium. Anode substrates tested on chemical stability in the CO_2 atmosphere showed high stability compared to anode substrates based on commonly used doped barium cerates. Microstructural properties of the anode pellets before and after testing in CO_2 were investigated using X-ray diffraction analysis. Impedance spectroscopy measurements were used for evaluation of electrical properties of the anode pellets and the conductivity values of reduced anodes of more than 14 S cm^{-1} at 600 °C confirmed percolations through Ni particles. Under fuel cell operating conditions, the cell with a Ni–BCIY20 anode achieved the highest performance, demonstrating a peak power density 223 mW/cm^2 at 700 °C confirming the functionality of Ni–BCIY anodes.

1. Introduction

Cermet anodes based on NiO and high temperature proton conductors (HTPCs) are used for the fabrication of intermediate temperature solid oxide fuel cells (IT-SOFCs) to reduce the large anode overpotential caused by decreasing of the operating temperature [1–7]. Reduction of NiO to Ni creates electronic conduction pathways and porosity in the anode needed for gas-phase diffusion. Both electronic conduction and porosity are significant for the functionality of a SOFC anode. Cermet anodes have a longer triple phase boundary compared to anodes made of precious metals. In this type of anodes electrochemical reactions are extended from the electrolyte/anode interface to the whole anode volume creating an ion pathway. Even though anode properties are very important for the performance of proton conducting fuel cells, only a few studies have been made of cermet anode materials based on HTPCs [1,5,6,8–15].

The research of proton conductivity in perovskite type materials started more than three decades ago. Proton conductors, such as rare earth doped $BaCeO_3$, have received increasing attention as promising electrolyte candidates in IT-SOFCs due to their low activation energy for proton conduction [16–20]. Despite the high proton conductivity of doped $BaCeO_3$, its poor chemical stability makes it inadequate for fuel cell applications, i.e. for fabrication of anodes and electrolytes. In a CO_2-rich atmosphere doped $BaCeO_3$ starts to decompose according to the following equation [22–24]:

$$BaO + CO_{2(g)} \iff BaCO_{3(s)} \quad (1)$$

and the occurrence of secondary phases in the microstructure will affect the electrical properties of doped $BaCeO_3$ and the efficiency of a fuel cell system. Exposure of anode materials to a CO_2-rich atmosphere only influences the ceramic component, while NiO (or Ni) remains unchanged [4,7]. Degradation of doped $BaCeO_3$ limits the usage of the best solid state proton conductor $BaCe_{1-x}Y_xO_{3-\delta}$ (BCY) for anode fabrication in applications where CO_2 appears as a product, mainly in SOFCs that use hydrocarbons as fuel [4,21,24].

An alternative HTPC is doped $BaZrO_3$ that has been found to be chemically more stable than $BaCeO_3$ [25,26]. On the other hand, the poor sinterability of barium zirconates leads to the presence of a large grain boundary resistance, resulting in lower electrical conductivity compared to doped barium cerates [22,27,28].

* Corresponding author. Tel.: +55 16 3301 9828.
E-mail address: milan@iq.unesp.br (M. Zunic).

0925-8388/$ - see front matter © 2013 Elsevier B.V. All rights reserved.
http://dx.doi.org/10.1016/j.jallcom.2013.02.122

One of the strategies for stabilization of BCY is partially substituting Zr for Ce [26,29] and some promising results were obtained in this area.

Another way to stabilize BCY is using dopants with a higher electronegativity and higher ionic radius compared to Ce and Y. According to the Lewis acid-base theory in solid oxide systems, the basicity at O of the metal–oxygen bond increases with the increase of the electropositive nature and the ionic radius of the metal [30]. In this respect, doping of BCY with elements that are more electronegative and have larger ionic radii than Ce and Y could elevate overall acidity of the crystal lattice and improve resistance against carbonatization induced by CO_2. It has been reported that BCY shows good stability when it is doped with elements that have the above mentioned properties (Nb, Ta or In), although with an inevitable decline in electrical properties [21,31–35]. At any rate, these results are encouraging and give a good base for further improvement of fuel cell components based on doped barium cerates.

In this work the main goals were to synthesize chemically stable anode substrates NiO–$BaCe_{0.9-x}In_xY_{0.1}O_{3-\delta}$ (NiO–BCIYx) and to investigate how the concentration of indium influences microstructural and electrical characteristics of anode substrates before and after reduction. The aim was also to confirm the functionality of these anode substrates by fuel cell tests of anode supported SOFC prototypes.

2. Experimental

The ceramic proton conductor materials $BaCe_{0.9-x}In_xY_{0.1}O_{3-\delta}$ (BCIY, where $x = 0.05$, 0.10, 0.15 and 0.20) were synthesized using the citrate–nitrate autocombustion method. Obtained powders are marked according to the concentration of indium as BCIY5, BCIY10, BCIY15 and BCIY20, respectively. Starting reactants were $Ba(NO_3)_2$ (Aldrich, 99.999%), $Ce(NO_3)_2{\cdot}6H_2O$ (Aldrich, 99.999%), $In(NO_3)_3{\cdot}5H_2O$ (Aldrich, 99.99%) and $Y(NO_3)_2{\cdot}6H_2O$ (Aldrich, 99.9%) and citric acid as the combustion fuel. The synthesis procedure has been described in detail elsewhere [36]. The obtained powders were fired at 1000 °C for 5 h and characterized by X-ray diffraction (XRD, Rigaku DMax 2500 PC) analysis and field emission scanning electron microscopy (FE-SEM, Jeol JSM 6330F).

NiO–$BaCe_{0.9-x}In_xY_{0.1}O_{3-\delta}$ (NiO–BCIY) cermet composite powders were prepared using the method of evaporation and decomposition of solution and suspensions (EDSS) [4,7] in order to obtain a uniform distribution of NiO grains in the BCIY ceramic. Anode compositions were marked as NiO–BCIY5, NiO–BCIY10, NiO–BCIY15 and NiO–BCIY20, according to the concentration of indium in the ceramic component. The starting reactants were $Ni(NO_3)_2{\cdot}6H_2O$ (Aldrich, 99.99%) and the already prepared BCIY compositions. The weight ratio between Ni and BCIY was 1:1. The resulting powders were milled in an agate mortar and calcined at 1000 °C for 5 h.

The anode slurry was prepared by mixing polyvinyl alcohol (PVA, Aldrich, 99.9%), NiO–BCIY cermet powders and corn starch (Duryea®) in water. Corn starch has the role of pore former and PVA has the role of binder. The weight ratio between cermet, corn starch, and PVA was 75:20:5, respectively. For electrical characterization, cylindrical anode pellets with a diameter of 12 mm and a thickness of about 0.5 mm were uniaxially pressed at 150 MPa and sintered at 1450 °C for 5 h. All samples were reduced in H_2 atmosphere at 700 °C for electrical characterization of reduced anode pellets.

Porosity of reduced samples was measured by the Archimedes method, using water as the fluid. Samples were dried out overnight and weighed to determine the dry weight. To increase water penetration for the submerged and wet sample measurements, samples were held under vacuum for 3 h before water was added.

The sintered anode pellets were exposed to CO_2 atmosphere at 700 °C for 24 h by keeping the flow rate of CO_2 through the aperture 50 cm^3/min. After being exposed the pellets were investigated by XRD analysis in order to determine the occurred phase changes.

Electrochemical impedance spectroscopy (EIS) measurements of anode pellets were performed using a FRA Solartron 1260, coupled with a Solartron 1296 dielectric interface in the range of temperatures from 550 to 700 °C and in the range of frequencies from 0.1 Hz to 5 MHz with the AC voltage amplitude of 50 mV before and after reduction in wet H_2. The impedance plots were fitted using ZView® for Windows software (Version 3.2b).

Prototypes of the fuel cells were produced using the method of co-pressing. Firstly, NiO–BCIY powders were uniaxially pressed at 70 MPa and then 10 mg of BCIY powder was distributed on the surface of the anode pellet. The NiO–BCIY/BCIY half cell was produced by uniaxially pressing at 150 MPa and co-sintering at 1450 °C for 5 h.

To make a complete fuel cell prototype, $La_{0.8}Sr_{0.2}Co_{0.8}Fe_{0.2}O_3$ (LSCF) with 10 wt.% of $BaCe_{0.7}In_{0.2}Y_{0.1}O_{3-\delta}$ (BCIY20) composite cathode powder mixed with commercial printing oil were paint brushed on BCIY dense electrolyte films and then fired at 1100 °C for 2 h. The diameter of the cathode electrode was 7 mm ($A = 0.385$ cm^2). Platinum wires were fixed with a drop of platinum paste (Engelhard-Clal) on the top of the anode and cathode and used as current collectors. For fuel cell tests, samples were mounted at the end of an alumina tube using a gas tight ceramic paste seal (Aremco, 552).

Hydrogen–air fuel cell experiments were carried out in the range of temperatures from 550 to 700 °C using Autolab PGSTAT302N (Eco Chemie BV). The anode was exposed to wet hydrogen (~3 vol.% H_2O) while the cathode was exposed to ambient air. The cell was equilibrated at an open-circuit for about 10 min before electrochemical measurements.

3. Results and discussion

The obtained anode powders prepared by the EDSS method were two phase systems without secondary phases. In Fig. 1, a XRD pattern of NiO–BCIY10 anode powder is shown as an example. Similar graphs were obtained for the other anode powders. All graphs showed the presence of two phases: NiO according to reference patterns JCPDS 78-0643 and the perovskite phase with orthorhombic lattice symmetry. These results suggest that the perovskite lattice structure was successfully doped with In as targeted, resulting in the formation of $BaCe_{0.9-x}In_xY_{0.1}O_{3-\delta}$. There have been several reports on indium-containing perovskite oxides [34,35,37].

Uniform distribution of anode components in the microstructure is a very important precondition for the proper functionality of anodes. The advantage of cermet composite anodes over metals with a high catalytic activity is a triple phase boundary extended to the whole anode volume. To provide proper catalytic functionality of cermet anodes the microstructure should consist of two continuous components: ceramics and Ni sublattice. SEM micrographs of NiO–BCIY5, NiO–BCIY10, NiO–BCIY15 and NiO–BCIY20 anodes sintered at 1450 °C for 5 h are shown in Fig. 2a–d, respectively. All compositions had similar microstructures with a good distribution of NiO and BCIY grains. The difference between these compositions was the average grain size (AGS) of the ceramic phase; while the AGS of the NiO phase was the same for all compositions (2.3 μm), the AGS of the BCIY phase increased with the amount of indium. The AGS of the ceramic component in NiO–BCIY5, NiO–BCIY10, NiO–BCIY15 and NiO–BCIY20 was 1.2, 1.5, 1.7 and 1.8 μm, respectively. This influence of indium on grain growth had been expected if we take into account that doping with indium improves sintering [35,38]. Different sintering behaviour of ceramic anode parts could result in different thermal expansion

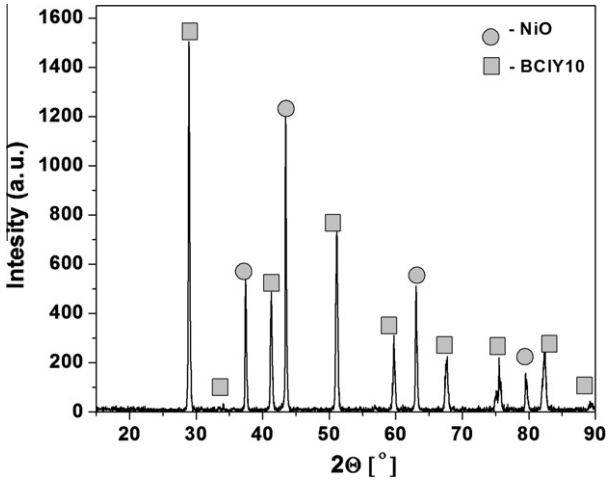

Fig. 1. XRD patterns of NiO–BCIY10 anode powder calcined at 1000 °C for 5 h.

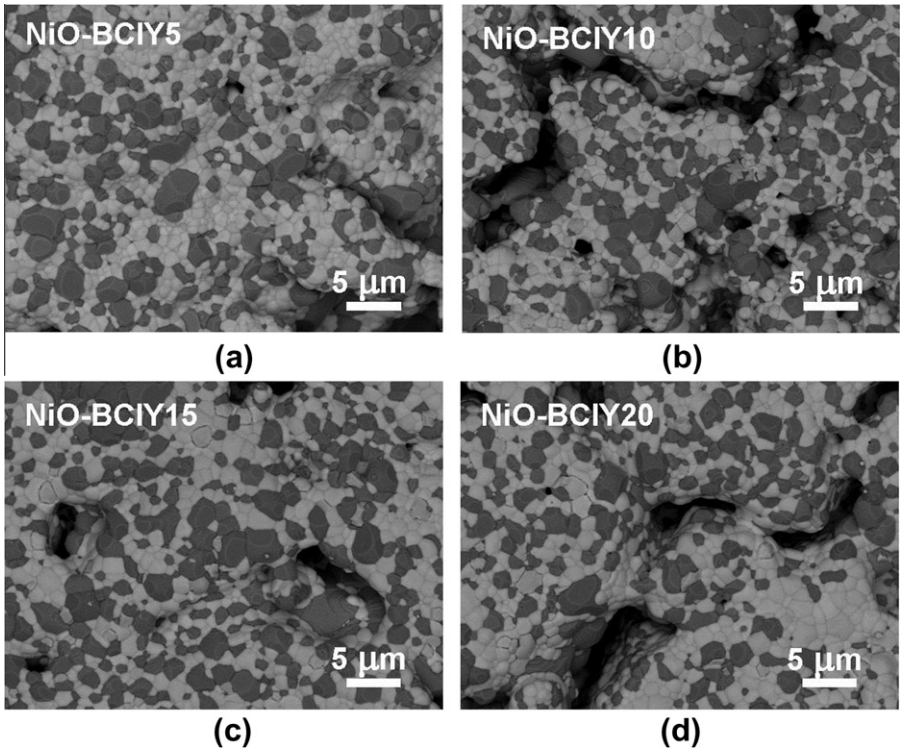

Fig. 2. SEM micrographs of anode pellets (a) NiO–BCIY5, (b) NiO–BCIY10, (c) NiO–BCIY15 and (d) NiO–BCIY20 sintered at 1450 °C for 5 h.

coefficients between microstructures. However, Fig. 2 shows that distribution of NiO and BCIY phases is not as good as distribution in some other anode compositions [4,7] obtained by the same method. This could cause poorer electrical properties of NiO–BCIY anodes compared to the NiO–BCY10 anodes.

Microstructures of anode samples after reduction in wet H_2 atmosphere at 700 °C are shown in Fig. 3a–d. In the anode microstructure pores could be formed in two ways: the first is burning of the pore former during sintering and the second is reduction of NiO to Ni in the reducing atmosphere at high temperatures. Burning of the pore former leaves large pores (Fig. 3a) which facilitate diffusion of fuel through the anode to the anode/electrolyte interface. During the reduction of NiO into Ni, around 41% reduction in volume of the NiO phase occurred [39]. This procedure leads to significant changes in the morphology and microstructure of the composite [40]. Oxygen diffused out of NiO and nickel particles shrank and formed a slit between them and the BCIY microstructure leaving long channels in the anode microstructure (Fig. 3a). Another consequence of oxygen diffusion was formation of nickel intragrain pores (Fig. 3a). If these pores are open channels or closed "pockets" is yet to be examined.

Reduction of samples decreased the initial volume of the NiO phase and the micrographs of cross-sections of samples in Fig. 3 illustrate a well connected subnet of BCIY grains and worse connectivity of Ni particles. Also, similar to non-reduced samples, with increasing indium content the volume ratio ceramic/metal increased, which could cause lower conductivity of Ni particles in anodes. However, the existence of percolation of Ni particles in the anode sample could only be confirmed by electrical measurements.

The porosity of anodes has an important role in the functionality of a fuel cell and it depends on the amount of pore former used [4,7]. In this work 20 wt.% of pore former was used according to our results from previous investigations of anode materials based on proton conductors [2,4,7]. In order to obtain an insight into porosity values of fabricated anodes, the porosities of Ni–BCIY15 and Ni–BCIY20 samples after reduction treatment were measured. For the Ni–BCIY15 sample, the measured porosity was 41% and for Ni–BCIY20 it was 44%, which should be sufficient porosity for gas transport of fuel.

Fig. 4a presents the XRD spectra of anode samples after sintering at 1450 °C for 5 h. It can be seen that all samples are characterized by two phases, without any additional phases. Fig. 4b shows the XRD patterns of anode samples after treatment in CO_2. The ceramic part of the anode with 5% of In shows chemical instability in CO_2 with the formation of CeO_2 (JCPDS 34-0394), $BaCO_3$ (JCPDS 71-2394), In_2O_3 (JCPDS 71-2194), $BaCeO_3$ (JCPDS 22-74) and Y_2O_3 (JCPDS 41-1105), while the NiO phase remains unchanged. However, comparing the stability of this anode that contains 5% of In with the stability of an anode without indium, such as NiO–$BaCe_{0.9}Y_{0.1}O_{3-\delta}$ [7], it is possible to conclude that In-doping increases stability of the anode's ceramic part based on $BaCe_{0.9}Y_{0.1}O_{3-\delta}$. NiO–BCIY anodes with 10%, 15% and 20% of In show relatively high resistance to CO_2 and the main phase of NiO–BCIY10, NiO–BCIY15 and NiO–BCIY20 samples remains unchanged. On the other hand, formation of $BaCO_3$ was observed in NiO–BCIY15 and NiO–BCIY20 samples after exposure to CO_2. It seems that doping with indium increases the stability of anode samples up to some point (less than 15% of indium) and that further increasing of the In content in anode samples leads again to a slight instability in the microstructure. Similar results were obtained by Bi et al. [3] when they worked with the $BaCe_{1-x}In_xO_{3-\delta}$ electrolyte. An explanation of increased stability could be found in the fact that the electronegativity of In is 1.78, which is much larger than Ce (1.12) and Y (1.22). This difference increases the acidity of the ceramic oxide and makes it more stable in an acidic environment. Further increasing of the In amount in the microstructure results in more oxygen vacancies leading to an increase in the ceramic oxide basicity [41]. The enlarged basicity will lead to an easier response to acidic gases, reducing the chemical stability in a CO_2 containing atmosphere.

The influence of the amount of indium on electrical characteristics of sintered anodes was examined using EIS measurements.

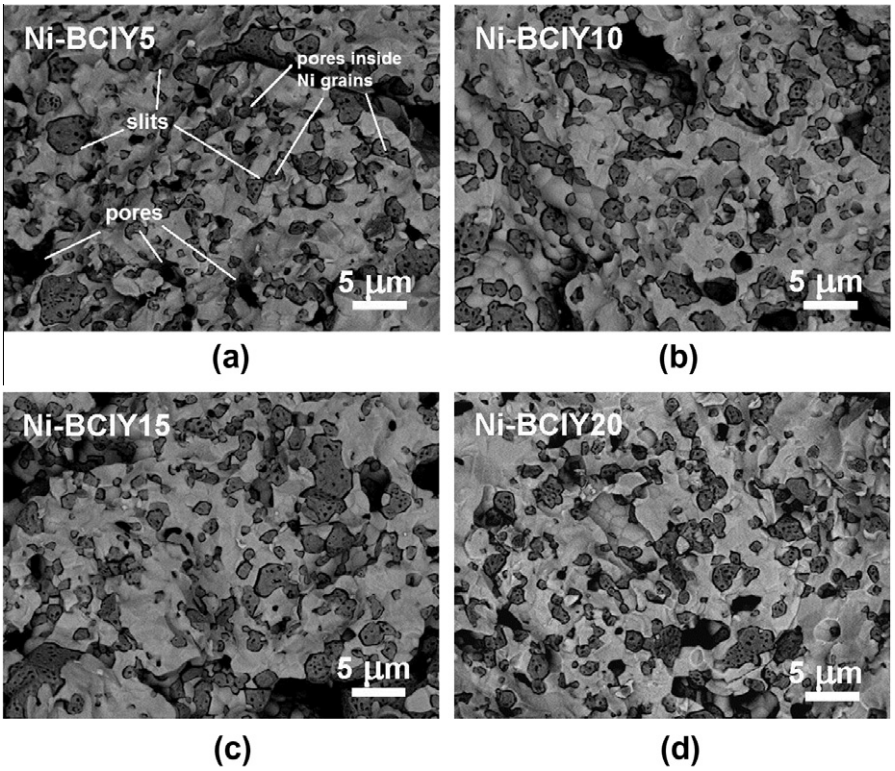

Fig. 3. SEM micrographs (cross-section view) of anode pellets (a) Ni–BCIY5, (b) Ni–BCIY10, (c) Ni–BCIY15 and (d) Ni–BCIY20 reduced in H_2 at 700 °C for 6 h.

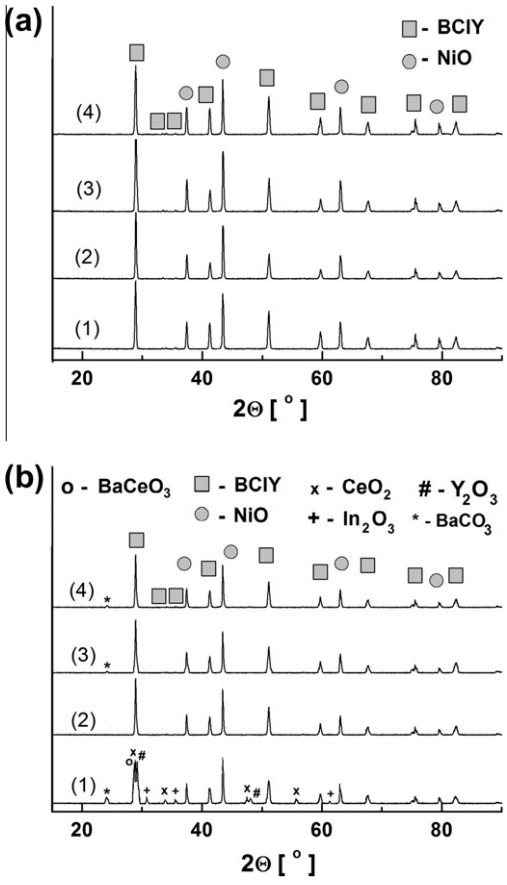

Fig. 4. XRD patterns of sintered anode samples: (1) NiO–BCIY5, (2) NiO–BCIY10, (3) NiO–BCIY15 and (4) NiO–BCIY20, before (a) and after (b) exposure to CO_2 atmosphere at 700 °C for 24 h.

Nyquist plots of a NiO–BCIY20 anode measured at different temperatures in wet Ar before reduction are shown in Fig. 5 as an example. The inset in Fig. 5 reports EIS measurements at 650 °C with an equivalent circuit and fitting curve. Similar plots with slightly depressed semicircles were also obtained for other anode samples. Inductance, L_1, resistors: R_1, R_2, R_3 and constant phase elements, denoted as CPE_1 and CPE_2 were used as elements of the equivalent circuit. The two constant phase elements are related to the two similar semicircles.

The real grain boundary capacitance, C, was calculated using the following equation [31,32]:

$$C = R^{\frac{1-n}{n}} Q^{\frac{1}{n}} \quad (2)$$

where Q and n represent the parameters of the constant phase elements and R is the resistivity of the grain boundary. The first arc (CPE_1) appeared in the high frequency region with a capacitance in the order of 10^{-9} F cm^{-1}, which is typical of grain boundary

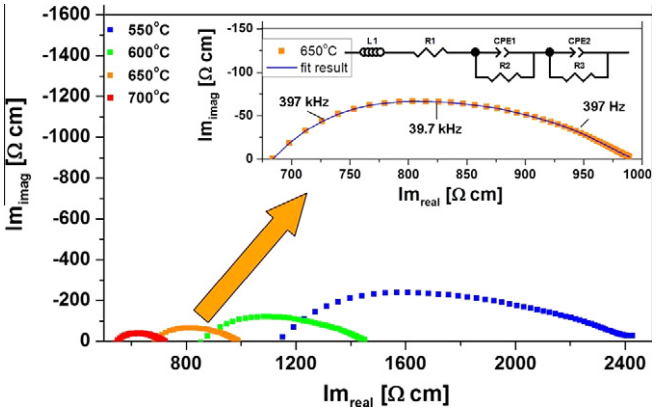

Fig. 5. Nyquist plots of NiO–BCIY20 sintered anode pellet measured before reduction at different temperatures in wet Ar.

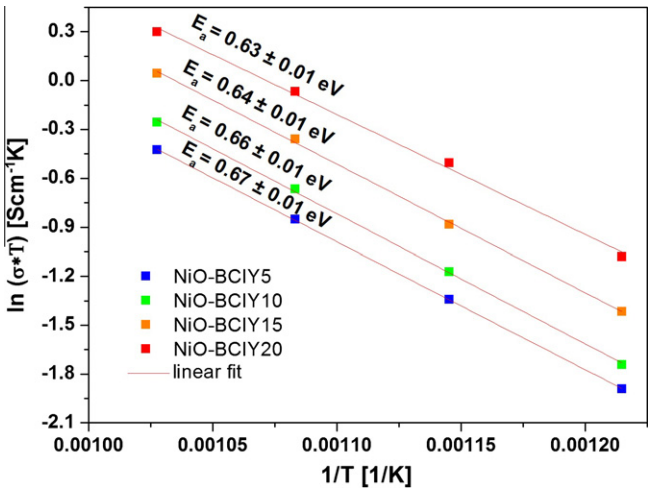

Fig. 6. Arrhenius plots of sintered anode samples at different temperatures, in Ar atmosphere before reduction treatment.

conductivity [42]. The second arc (CPE_2) in the intermediate frequency range was related to a capacitance in the order of 10^{-6}-F cm^{-1}, which was associated with processes at the electrode/electrolyte interface [43]. Separate contributions of NiO and BCIY could not be resolved from impedance spectra.

The total resistance of the sample determined from the impedance spectra is the sum of $R_{total} = R_b + R_{gb}$, where R_b is the bulk resistance and R_{gb} is the grain boundary resistance.

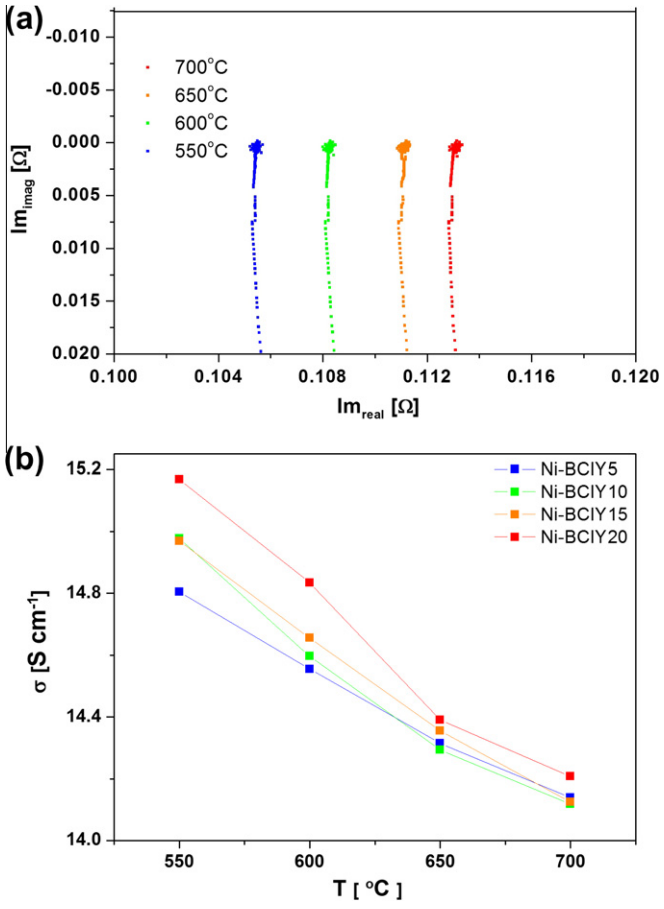

Fig. 7. (a) Nyquist plots of sintered anode samples and (b) conductivities of anode sintered samples at different temperatures, in wet H_2 atmosphere after reduction treatment.

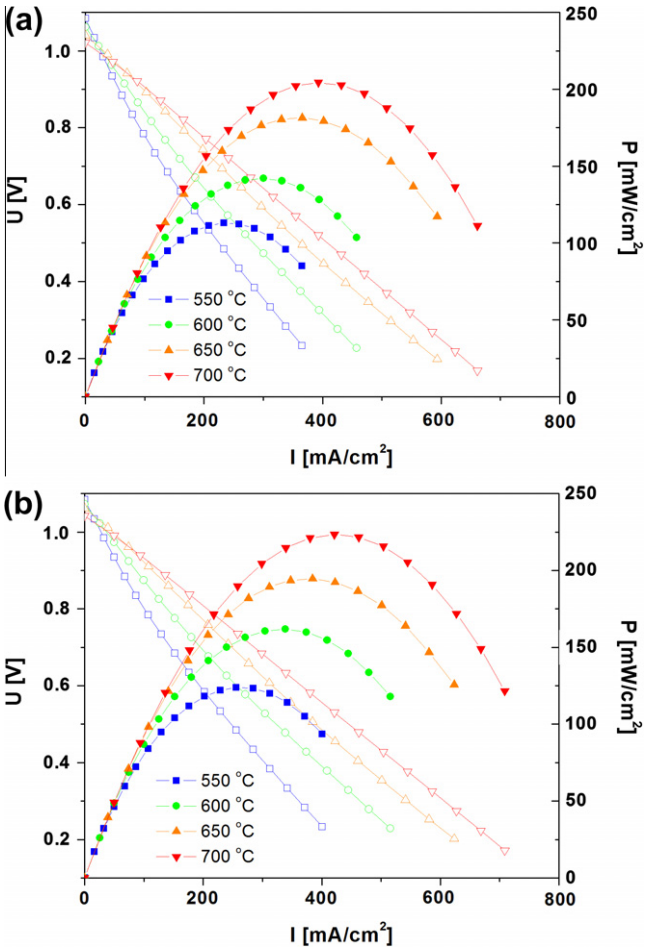

Fig. 8. *I–V* curves and power outputs of: (a) Ni–BCIY15/BCIY15/LSCF–10BCIY (FC15) and (b) Ni–BCIY20/BCIY20/LSCF–10BCIY (FC20) measured at different temperatures in hydrogen–air fuel cell experiments.

Fig. 6 shows Arrhenius plots extracted from the values of total resistances in EIS measurements for sintered anode pellets in Ar atmosphere before reduction treatment. Conductivity in wet Ar of NiO–BCIY sintered pellets is thermally activated with activation energy (Ea) of around 0.65 eV, which is attributed to the BCIY component of the pellet. This assumption was based on the fact that NiO is a p-type semiconductor with the activation energy Ea = 0.1–0.4 eV and showed a very low conductivity in the investigated temperature range (550–700 °C) [4,44]. To confirm this assumption it would be necessary to compare values of the ionic and electronic conductivity. This figure also shows the slight decreasing of activation energies with the increasing of amount of indium in the samples. The conductivities of sintered pellets are in the order of magnitude 10^{-3} S cm^{-1} at 650 °C, indicating a high ionic conduction through the whole composite pellet. This behaviour demonstrated a well interconnected BCIY sintered network, in agreement with the microstructural analysis shown in Fig. 2. The values of anode conductivities increased with the increase of the amount of indium. Doping with trivalent indium oxide introduces ion vacancies in the crystal structure that permits dissociative absorption of water to facilitate proton conduction [17]. The increase of the doping level of In forms a higher protonic defect concentration, leading to higher proton conductivity [45].

In Fig. 7a EIS plots for reduced Ni–BCIY pellets are shown. The values of real impedance increase with the increasing of temperature indicating metallic conductivity. For the reduced samples the amount of indium has no influence on conductivity. The

Table 1
Values of *OCV* and maximal power density output for samples tested at different temperatures.

Samples	*OCV* (V)				*P* (mW/cm^2)			
	550 °C	600 °C	650 °C	700 °C	550 °C	600 °C	650 °C	700 °C
FC15	1.08	1.06	1.04	1.02	113	142	181	204
FC20	1.08	1.07	1.06	1.04	123	161	194	223

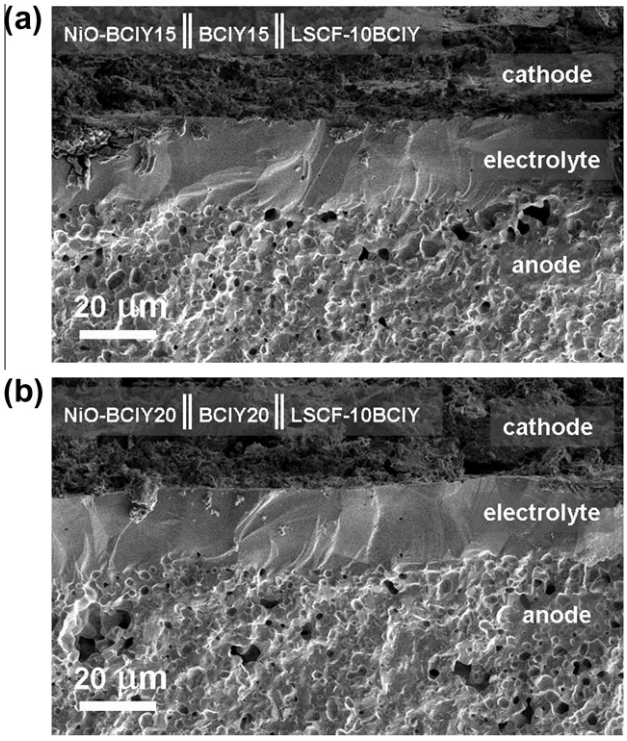

Fig. 9. SEM micrograph (cross-section view) of the FC15 (a) and (b) FC20 prototype cell after fuel cell experiments.

dependence of the conductivity values on temperature of all samples is presented in Fig. 7b. The calculated values are in the range 14–15 S cm^{-1}, confirming that percolation through Ni particles took place properly.

In order to examine the functionality of anode samples, two prototypes of fuel cells were made: NiO–BCIY15||BCIY15||LSCF–10BCIY (marked as FC15) and NiO–BCIY20||BCIY20||LSCF–10BCIY (marked as FC20). When fabricating fuel cell prototypes the ceramic part of the anode had the same composition as the electrolyte aiming to reduce thermal mismatch and to avoid cracks in the electrolyte during co-sintering of the anode/electrolyte bi-layer. Fabrication of fuel cells prototypes using the method of co-pressing was possible due to a large volume of electrolyte powders obtained by the auto-combustion method. A small amount of these powders (10 mg) was distributed uniformly on the anode substrate surface.

Fig. 8a and b shows *I–V* curves and the power density output of cells FC15 and FC20, respectively, obtained by exposing the anode to wet H_2 and the cathode to ambient air in the range of temperatures from 550 to 700 °C. For both fuel cells the measured open circuit voltage (*OCV*) values at different temperatures are lower but still close to the theoretical values. The FC15 cell had the maximum power density 204 mW/cm^2, while FC20 had the maximum power density 223 mW/cm^2 at the temperature of 700 °C. All measurement results are summarized in Table 1.

Fig. 9a and b shows SEM cross-section micrographs of FC15 and FC20 fuel cells after electrochemical measurements. No major degradation effects are visible. The three materials components of the fuel cell are clearly identified. Both cathode–electrolyte and anode–electrolyte interfaces show good interfacial adhesion. Electrolyte thicknesses of both samples are 21 μm ± 1 μm.

Considering that the electrical properties of anodes with 15% and 20% of indium are very similar, the slightly better performances of FC20 could be ascribed to higher concentrations of proton defects in the BCIY20 electrolyte and better sinterability of the BCIY20 electrolyte, which is the consequence of the higher amount of indium in the microstructure. Also, the slightly higher values of *OCV* of sample FC20 at temperatures 600–700 °C confirm that the BCIY20 electrolyte layer is denser compared to BCIY15.

Although the results of fuel cell tests could be enhanced by further investigation of the interfacial polarization resistance and anode composition, these results confirmed the functionality of NiO–BCIY proton conducting cermet anodes. Future investigations on this subject will be oriented to the influence of porosity and nickel amount on the electrical properties of NiO–BCIY anodes.

4. Summary and conclusions

Porous anode substrates NiO–$BaCe_{0.9-x}In_xY_{0.1}O_{3-\delta}$ with different amounts of In were synthesized without the presence of secondary phases. The sample porosity was in the range 40–45%. Testing of chemical stability in CO_2 showed that indium content up to approximately 15 wt.% increased the stability of anode samples. Further increase of In content in anode samples again induced a slight instability in the microstructure. Microstructural analysis revealed good connectivity of the ceramic part and fair connectivity of nickel particles. Electrical measurements of anode samples before reduction showed that with increase in the doping level of indium the conductivity values of sintered non-reduced anode samples increased. The values of conductivities ($\sim 10^{-3}$ S cm^{-1} at 650 °C) and the values of activation energies ($\sim$0.65 eV) of the anode samples before reduction demonstrated well interconnected BCIY grains. Even though microstructural analysis showed fair connectivity of Ni particles in the microstructure, the conductivity values ($\sigma^* > 14$ S cm^{-1}) of all samples after reduction confirmed that percolation through Ni particles took place properly. The functionality of anodes was demonstrated by fuel cell tests. Prototypes of fuel cells with an anode that contained 15% of indium (FC15) showed the maximum power density 204 mW/cm^2 and prototypes with an anode that contained 20% of indium (FC20) showed the maximum power density 223 mW/cm^2 at the temperature of 700 °C. This slight difference in fuel cell performance could be attributed to better sinterability and higher concentration of proton defects in the BCIY20 electrolyte as a consequence of the higher amount of indium in the microstructure. Also, the slightly higher values of *OCV* of sample FC20 at temperatures 600–700 °C confirmed that the BCIY20 electrolyte layer was denser compared to BCIY15. Further investigations on the interfacial polarization resistance between the anode and electrolyte and on anode composition are required in order to improve the functionality of fuel cells.

Acknowledgements

The authors acknowledge that this work was supported by the Fundacão de Amparo à Pesquisa do Estado de Saõ Paulo-FAPESP

(Project No. 2010/20574–3), CNPq, CAPES and Ministry of Education and Science of the Republic of Serbia (Project No. III45007). The authors also appreciate the valuable help of Prof. Dr. Márcio de Sousa Góes and his FAPESP Project No. 2009/14713-3.

References

[1] L. Yan, W. Sun, L. Bi, S. Fang, Z. Tao, W. Liu, J. Alloys Comp. 508 (2010) L5.
[2] M. Zunic, L. Chevallier, F. Deganello, A. D'Epifanio, S. Licoccia, E. Di Bartolomeo, E. Traversa, J. Power Sources 190 (2009) 417.
[3] A.A. Fakhrabadi, R.E. Avila, H.E. Carrasco, S. Ananthakumar, R.V. Mangalaraja, J. Alloys Comp. 541 (2012) 1.
[4] L. Chevallier, M. Zunic, V. Esposito, E. Di Bartolomeo, E. Traversa, Solid State Ionics 180 (2009) 715.
[5] C.-K. Cho, B.-H. Choi, K.-T. Lee, J. Alloys Comp. 541 (2012) 433.
[6] L. Bi, E. Fabbri, E. Traversa, Electrochem. Commun. 16 (2012) 37.
[7] M. Zunic, L. Chevallier, A. Radojkovic, G. Brankovic, Z. Brankovic, E. Di Bartolomeo, J. Alloys Comp. 509 (2011) 1157.
[8] P. Ranran, W. Yan, Y. Lizhai, M. Zongqiang, Solid State Ionics 177 (2006) 389.
[9] N. Maffei, L. Pelletier, A. McFarlan, J. Power Sources 136 (2004) 24.
[10] T.H. Lee, S.E. Dorris, U. Balachandran, Solid State Ionics 176 (2005) 1479.
[11] J. Le, L.N. van Rij, J. Schoonman, J. Electrochem. Soc. 147 (2000) 4345.
[12] S. Fang, L. Bi, C. Yang, L. Yan, C. Chen, W. Liu, J. Alloys Comp. 475 (2009) 935.
[13] X. Zhu, Q. Zhong, D. Xu, H. Yan, W. Tan, J. Alloys Comp. 555 (2013) 169.
[14] G.C. Mather, D.P. Fagg, A. Ringuedé, J.R. Frade, Fuel Cells 1 (2001) 233.
[15] M.L. Fontaine, Y. Larring, R. Haugsrud, T. Norby, K. Wiik, R. Bredesen, J. Power Sources 188 (2009) 106.
[16] T. Norby, Solid State Ionics 125 (1999) 1.
[17] K.D. Kreuer, Annu. Rev. Mater. Res. 33 (2003) 333.
[18] W.A. Meulenberg, J.M. Serra, T. Schober, Solid State Ionics 177 (2006) 2851.
[19] S.Y. Wang, J.L. Luo, A.R. Sanger, K.T. Chuang, J. Phys. Chem. C 111 (2007) 5069.
[20] L. Bi, S.Q. Zhang, S.M. Fang, L. Zhang, K. Xie, C.R. Xia, W. Liu, Electrochem. Commun. 10 (2008) 1005.
[21] L. Bi, E. Fabbri, Z. Sun, E. Traversa, Solid State Ionics 196 (2011) 59.
[22] K.H. Ryu, S.M. Haile, Solid State Ionics 125 (1999) 355.
[23] S. Yamaguchi, K. Nakamura, T. Higuchi, S. Shin, Y. Iguchi, Solid State Ionics 136–137 (2000) 191.
[24] N. Zakowsky, S. Williamson, J.T.S. Irvine, Solid State Ionics 176 (2005) 3019.
[25] A. D'Epifanio, E. Fabbri, E. Di Bartolomeo, S. Licoccia, E. Traversa, Fuel Cells 8 (2008) 69.
[26] E. Fabbri, A. D'Epifanio, E. Di Bartolomeo, S. Licoccia, E. Traversa, Solid State Ionics 179 (2008) 558.
[27] K. Katahira, Y. Kohchi, T. Shimura, H. Iwahara, Solid State Ionics 138 (2000) 91.
[28] S.M. Haile, G. Staneff, K.H. Ryu, J. Mater. Sci. 36 (2001) 1149.
[29] S.-W. Lee, C.-J. Tseng, J.-K. Chang, K.-R. Lee, C.-T. Chen, I.-M. Hung, S.-L. Lee, J.-C. Lin, J. Alloys Comp. (2013). http://dx.doi.org/10.1016/j.jallcom.2013.01.101.
[30] A. Zecchina, C. Lamberti, S. Bordiga, Catalysis Today 41 (1998) 169.
[31] A. Radojković, M. Žunić, S.M. Savić, G. Branković, Z. Branković, Ceram. Int. 39 (2013) 307.
[32] A. Radojković, M. Žunić, S.M. Savić, G. Branković, Z. Branković, Ceram. Int. 39 (2013) 2631.
[33] E. Di Bartolomeo, A. D'Epifanio, C. Pugnalini, F. Giannici, A. Longo, A. Martorana, S. Licoccia, J. Power Sources 199 (2012) 201.
[34] F. Zhao, Q. Liu, S. Wang, K. Brinkman, F. Chen, Int. J. Hydrogen Energy. 35 (2010) 4258.
[35] L. Bi, S. Zhang, L. Zhang, Z. Tao, H. Wang, W. Liu, J. Hydrogen Energy. 34 (2009) 2421.
[36] F. Deganello, G. Marcì, G. Deganello, J. Eur. Ceram. Soc. 29 (2009) 439.
[37] I. Ahmed, S.-G. Eriksson, E. Ahlberg, C.S. Knee, P. Berastegui, L.-G. Johansson, H. Rundlöf, M. Karlsson, A. Matic, L. Börjesson, D. Engberg, Solid State Ionics 177 (2006) 1395.
[38] H.-J. Gau, J.-L. Yu, C.-C. Wu, Y.-K. Kuo, C.-H. Ho, J. Alloys Comp. 480 (2009) 73.
[39] T. Suzuki, Z. Hasan, Y. Funahashi, T. Yamaguchi, Y. Fujishiro, M. Awano, Science 325 (2009) 852.
[40] M.J. -Melendo, M.O. -Ramírez, F.A.H. -Mamani, J. Alloys Comp. 536 (2012) S472.
[41] H. Matsumoto, Y. Kawasaki, N. Ito, M. Enoki, T. Ishihara, Electrochem. Solid State Lett. 10 (2007) B77.
[42] T.S. Bjorheim, A. Kuwabara, I. Ahmed, R. Haugsrud, S. Stolen, T. Norby, Solid State Ionics 181 (2010) 130.
[43] V. Dusastre, J.A. Kilner, Solid State Ionics 126 (1999) 163.
[44] F.C. Fonseca, D.Z. de Florio, V. Esposito, E. Traversa, E.N.S. Muccillo, R. Muccillo, J. Electrochem. Soc. 153 (2006) A354.
[45] F. Giannici, A. Longo, A. Balerna, K.D. Kreuer, A. Martorana, Chem. Mater. 19 (2007) 5714.